Chemical Engineering Journal 160 (2010) 293–301

Contents lists available at ScienceDirect

Chemical Engineering Journal

journal homepage: www.elsevier.com/locate/cej

Assessment of CFD Euler–Euler method for trickle-bed reactor modelling in the catalytic wet oxidation of phenolic wastewaters

Rodrigo J.G. Lopes*, Rosa M. Quinta-Ferreira

GERSE – Group on Environmental, Reaction and Separation Engineering, Department of Chemical Engineering, University of Coimbra, Rua Sílvio Lima, Polo II – Pinhal de Marrocos, 3030-790 Coimbra, Portugal

ARTICLE INFO

Article history:
Received 6 August 2009
Received in revised form 10 March 2010
Accepted 12 March 2010

Keywords:
Computational fluid dynamics
Euler–Euler model
Multiphase flow
Dynamic behaviour

ABSTRACT

Trickle-bed reactors (TBRs) are envisaged as a breakthrough technology in industrial wastewater treatment plants. According to the literature, the generous research in environmental reaction engineering has indicated that scale-up of TBR is erroneous if one considers isothermal operation and uses either a pseudo-homogeneous or a heterogeneous model with plug flow for gas and liquid phases. Even though axial dispersion model may account for liquid distribution non-uniformity, the reaction parameters are strongly dependent on the reactor fluid dynamics.

In our case study, we develop an Eulerian CFD (computational fluid dynamics) framework based on empirical interphase coupling parameters in the momentum balance equation. After the hydrodynamic validation, the catalytic wet oxidation of phenolic wastewaters was taken as an example to evaluate axial and radial profiles for the total organic carbon depletion and temperature along the packed bed. The theoretical calculations were compared against experimental data taken from a trickle-bed reactor pilot plant. The Eulerian computations have shown promising results on how fluid dynamics can be correlated with chemical reaction, namely on the prediction of total organic carbon conversions attained at different temperatures.

1. Introduction

Bisphenols, alkylphenols, trihydroxybenzenes, hydroxybiphenyls, catechols and phenol ethers belong to a class of toxic organic compounds listed by the EPA (Environmental Protection Agency) as priority pollutants. These compounds often contaminated the natural water bodies and are produced in the petrochemical, pharmaceutical, pesticide, dye and agro-industries. Phenol derivatives are characterized by their toxicity, difficulty and persistency at the time of water decontamination. Consequently, highly efficient techniques such as photocatalytic and sonochemical degradation, Fenton oxidation, ozonation, microwave irradiation, supercritical water oxidation and wet air oxidation (WAO) are advanced oxidation techniques, which mineralize organics to harmless final products using appropriate catalysts [1–7].

Among these alternative destruction technologies, catalytic wet air oxidation (CWAO) has been used in the treatment of wastewaters containing either moderately concentrated non-toxic or bio-toxic organic pollutants. The biological refractory pollutants are oxidised by dissolved molecular oxygen which can be further accelerated with a homogeneous or heterogeneous catalysts. However, the industrial application of CWAO has been controlled by the scarce development of catalysts that are stable at high operating values of temperature and pressure [8]. The recent development of economical and stable catalysts is an encouraging factor concerning the catalyst deactivation and the formation of carbonaceous deposits that hampers the access to the catalyst sites. The selection of a suitable reactor in another key criterion that can affect the industrial implementation of advanced wastewater treatment facilities. While most laboratory studies have been carried out in slurry and/or fixed-bed reactors, recent comparisons between those operating configurations have demonstrated that fixed-bed reactors are advantageous either in terms of process selectivity or stability. While agitated reactors (slurry or spinning basket) exhibited higher liquid-to-catalyst ratio promoting negatively parallel homogeneous polymerisation reactions, fixed-bed reactors in CWAO emerged as the best choice for systems with high potential for polymerisation reactions [9,10]. According to several experimental studies on activated carbon, the increasing catalyst activity loss and lower selectivity towards complete mineralization strongly affects the organic carbon decontamination rates when one operates with batch stirred vessels [10]. Nevertheless, Maugans and Akgerman [11] among other researchers have shown that total organic carbon (TOC) depletion rates in a co-current fixed-bed reactor can be successfully

* Corresponding author. Tel.: +351 239798723; fax: +351 239798703.
E-mail address: rodrigo@eq.uc.pt (Rodrigo J.G. Lopes).

1385-8947/$ – see front matter © 2010 Elsevier B.V. All rights reserved.
doi:10.1016/j.cej.2010.03.024

Nomenclature

C_μ, $C_{1\varepsilon}$, $C_{2\varepsilon}$	k–ε model parameters: 0.09, 1.44, 1.92
C	specie concentration (ppm)
d_p	catalyst particle nominal diameter (m)
E_1, E_2	Ergun's constants: 180, 1.75
$\vec{g}$	gravitational acceleration, 9.81 m/s^2
G	gas mass flux (kg/m^2 s)
G_{kL}	generation rate of turbulent kinetic energy
K_{pq}	interphase momentum exchange term
k	k–ε model kinetic energy
k'	apparent reaction rate constant
L	liquid mass flux (kg/m^2 s)
p	pressure (bar)
$-r$	oxidation rate
$S_{q,i}$	source mass of specie i for phase q (ppm)
$S_{q,h}$	source term containing volumetric reaction heat (J)
t	time (s)
T	temperature (°C)
TOC	total organic carbon (ppm)
$\vec{u}$	superficial vector velocity (m/s)

Greek letters

α_q	volume fraction of qth phase
ε	k–ε model dissipation energy
ρ_q	density of qth phase (kg/m^3)
Δp	total pressure drop (Pa)
σ	surface tension coefficient
σ_k, σ_ε	k–ε model parameters: 1.2, 1.0
τ	residence time (s)
$\overline{\overline{\tau_q}}$	viscous stress tensor of qth phase (Pa)
μ_q	viscosity of qth phase (Pa s)

Subscripts

G	gas phase
i	lumped specie
q	qth phase
L	liquid phase
S	solid phase

Supercripts

t^*	dimensionless time $[t/\tau]$

predicted with kinetic expressions obtained from batch reaction studies.

Experimental studies on CWAO indicated that trickle-bed reactors have often been implemented in contrast with other operation modes for gas–liquid–solid reactions [10,12–15]. In this ambit, three important hydrodynamic parameters, two-phase pressure drop, total liquid holdup and axial dispersion have been selected as the major benchmarking parameters in the comparison of both operation modes. Two-phase pressure drop and total liquid holdup are higher for the upflow mode of operation at lower gas and liquid velocities, but with increasing flow rates, the two parameters were comparable for upflow and downflow modes as stated by Chander et al. [16]. Saroha and Khera [17] demonstrated that the values of Peclet number were higher in downflow mode of operation for the entire range of flow rates studied indicating the presence of lower backmixing in the downflow mode of operation, and a comparison of the experimental observation with the correlations available in the literature is also presented.

One should also bear in mind that the design rules of multiphase reactors are still weak and, for this reason, sophisticated scale-up procedures based on modern computational fluid dynamic (CFD) codes have received much more attention during the last decade [18]. Given that traditional scale-up procedures are prone to more uncertainty and it is not possible in general to relate via simple scale-up rules the performance of laboratory size units to large-scale reactors, further investigation of CWAO kinetics in another reactor types coupled with and CFD models of the large units is usually becoming the preferred route in process development. CFD shows promising results in understanding fluid dynamics and its interactions with chemical reactions. Gunjal and Ranade [19] have developed a CFD model for simulating flow and reactions in the laboratory scale and commercial scale hydro-processing reactors. The CFD models were first evaluated by comparing the model predictions with the published experimental data. The models were then used to understand the influence of porosity distribution, particle characteristics and reactor scale on overall performance and the validated model was used to predict the performance of the commercial scale reactor.

CFD models based on Eulerian codes are being constantly developed in order to gain a deep understanding on how the hydrodynamic parameters affect the performance of trickle-bed reactors. Lopes and Quinta-Ferreira [20] presented an Euler–Euler model and solved it for a three-dimensional representation of the catalytic bed. The Eulerian multiphase model was successfully used in the computation of pressure drop and liquid holdup and over a wide range for the calculated flow regime as a function of gas and liquid flow rates, the CFD theoretical predictions were in good agreement for both hydrodynamic parameters. Later, Lopes and Quinta-Ferreira [21] studied the interstitial phenomena and several computations on multiphase flow distribution have been accomplished querying the effect of gas and liquid flow rate on overall hydrodynamics. Lopes and Quinta-Ferreira [22] also investigated turbulence phenomena with four RANS multiphase turbulence models. The authors have found that standard k–ε dispersed turbulence model gave the better compromise between computer expense and numerical accuracy in comparison with both realizable, renormalization group and Reynolds stress based models. Several computational runs were performed at different temperatures for the evaluation of both axial averaged velocity and turbulent kinetic energy profiles for gas and liquid phases. Flow disequilibrium and strong heterogeneities detected along the packed bed demonstrated liquid distribution issues with slighter impact at higher temperatures.

It is well known that various critical issues arise in TBR scale-up if one is only concerned with hydrodynamics. CFD models have also to be validated at reacting flow conditions which can improve the global understanding of further industrial application of CWAO. From the above survey and to the best of our knowledge, no experimental study on CWAO has been correlated with CFD at reaction conditions. The Eulerian simulations carried out so far have been addressed the hydrodynamics and, with the present contribution, the Euler–Euler model computations and experimental data are presented here for the sake and completeness of CFD validation. This task will be useful for understanding the complex hydrodynamics, its interaction with chemical reactions and influence of different reactor scales on performance of trickle-bed reactors.

2. CFD model

2.1. Euler–Euler conservation equations

The mass conservation equation for each phase is expressed in Eq. (1):

$$\frac{\partial}{\partial t}(\alpha_q \rho_q) + \nabla \cdot (\alpha_q \rho_q \vec{u}_q) = 0 \quad (1)$$

Liquid and gas phases are assumed to share void space in proportion to their volumes leading to the unitary sum of volume fractions

in the cells domain: $\alpha_L + \alpha_G = 1$. The momentum conservation equation for the phase q after averaging is written in Eq. (2) and the respective tensor in Eq. (3):

$$\frac{\partial}{\partial t}(\alpha_q \rho_q \vec{u}_q) + \nabla \cdot (\alpha_q \rho_q \vec{u}_q \vec{u}_q) = -\alpha_q \nabla p + \nabla \cdot \bar{\bar{\tau}}_q + \alpha_q \rho_q \vec{g} + \sum_{p=1}^{n} (\vec{R}_{pq} + \dot{m}_{pq}\vec{u}_{pq} - \dot{m}_{qp}\vec{u}_{qp}) \quad (2)$$

$$\bar{\bar{\tau}}_q = \alpha_q \mu_q (\nabla \vec{u}_q + \nabla \vec{u}_q^T) + \alpha_q \left(\lambda_q - \frac{2}{3}\mu_q\right) \nabla \cdot \vec{u}_q \bar{\bar{I}} \quad (3)$$

Here μ_q ($\mu_q = \mu_{l,q} + \mu_{t,q}$) and λ_q are the shear and bulk viscosity of phase q. The interphase force, $\vec{R}_{pq}$, depends on the friction, pressure, cohesion, and other effects; it conforms to the conditions that $\vec{R}_{pq} = -\vec{R}_{qp}$ and $\vec{R}_{qq} = 0$ being possible to express a simple interaction term by Eq. (4):

$$\sum_{p=1}^{n} \vec{R}_{pq} = \sum_{p=1}^{n} K_{pq}(\vec{u}_p - \vec{u}_q) \quad (4)$$

where $K_{pq} = K_{qp}$ is the interphase momentum exchange coefficient.

2.2. Closure laws for gas–liquid–solid drag

The incomplete understanding of the governing physical laws in multiphase reactors plus the nonlinear coupled nature of the equations make the complete solution largely dependent in the mechanistic principles so that closure equations for gas–liquid–solid interactions integrated in the overall momentum balance equation are often approximations based on theoretical assumptions much in the same way as pressure drop in packed-bed flow is often correlated using Ergun equation [23]. Taking into account the model of Attou and Ferschneider [24], the interphase coupling terms are expressed in terms of interstitial velocities and phase volume fractions for gas–liquid, gas–solid and liquid–solid momentum exchange forms as expressed in Eqs. (5)–(7):

$$K_{GL} = \alpha_G \left(\frac{E_1 \mu_G (1-\alpha_G)^2}{\alpha_G^2 d_p^2} \left[\frac{\alpha_S}{1-\alpha_G}\right]^{2/3} + \frac{E_2 \rho_G (u_G - u_L)(1-\alpha_G)}{\alpha_G d_p} \times \left[\frac{\alpha_S}{1-\alpha_G}\right]^{1/3} \right) \quad (5)$$

$$K_{GS} = \alpha_G \left(\frac{E_1 \mu_G (1-\alpha_G)^2}{\alpha_G^2 d_p^2} \left[\frac{\alpha_S}{1-\alpha_G}\right]^{2/3} + \frac{E_2 \rho_G u_G (1-\alpha_G)}{\alpha_G d_p} \times \left[\frac{\alpha_S}{1-\alpha_G}\right]^{1/3} \right) \quad (6)$$

$$K_{LS} = \alpha_L \left(\frac{E_1 \mu_L \alpha_S^2}{\alpha_L^2 d_p^2} + \frac{E_2 \rho_L u_G \alpha_S}{\alpha_L d_p} \right) \quad (7)$$

2.3. Enthalpy and species continuity equations

The reactor gas–liquid mass transfer coefficient was determined by the correlations proposed by Larachi et al. [25]. The conservation of energy in Eulerian multiphase applications is described by a separate enthalpy equation for each phase as expressed in Eq. (8):

$$\frac{\partial}{\partial t}(\alpha_q \rho_q h_q) + \nabla \cdot (\alpha_q \rho_q \vec{u}_q h_q) = -\alpha_q \frac{\partial p}{\partial t} + \bar{\bar{\tau}}_q : \nabla \vec{u}_q - \nabla \cdot (k_{eff} \nabla T)_q + \sum_{p=1}^{n} (\dot{m}_{pq} h_{pq} - \dot{m}_{qp} h_{qp}) + S_{q,h} \quad (8)$$

The species continuity equation is expressed in Eq. (9):

$$\frac{\partial \alpha_q \rho_q C_{q,i}}{\partial t} + \nabla \cdot (\alpha_q \rho_q u_q C_{q,i}) = \nabla \cdot (\alpha_q \rho_q D_{q,i} \nabla C_{q,i}) + \alpha_q \rho_q S_{q,i} \quad (9)$$

2.4. Turbulence modelling

As the Reynolds numbers range is wide (min: 10, max: 2500), the multiphase k–ε model is used for turbulence modelling [26]. For incompressible flows, the turbulent liquid viscosity $\mu_{t,L}$ is given in Eq. (10):

$$\mu_{t,L} = \rho_L C_\mu \frac{k_L^2}{\varepsilon_L} \quad (10)$$

Turbulence parameters are obtained from the prediction of the transport equations for the k_L, kinetic energy, and ε_L, dissipation energy, written in Eqs. (11) and (12), respectively:

$$\frac{\partial}{\partial t}(\rho_L \alpha_L k_L) + \nabla \cdot (\rho_L \alpha_L \vec{u}_L k_L) = \nabla \cdot \left(\alpha_L \frac{\mu_{t,L}}{\sigma_k} \nabla k_L\right) + \alpha_L G_{k,L} - \alpha_L \rho_L \varepsilon_L + \alpha_L \rho_L \Pi_{kL} \quad (11)$$

$$\frac{\partial}{\partial t}(\rho_L \alpha_L \varepsilon_L) + \nabla \cdot (\rho_L \alpha_L \vec{u}_L \varepsilon_L) = \nabla \cdot \left(\alpha_L \frac{\mu_{t,L}}{\sigma_\varepsilon} \nabla \varepsilon_L\right) + \alpha_L \frac{\varepsilon_L}{k_L} \times (C_{1\varepsilon} G_{k,L} + C_{2\varepsilon} \rho_L \varepsilon_L) + \alpha_L \rho_L \Pi_{\varepsilon L} \quad (12)$$

2.5. Simulation set-up

The discretization of the governing equations was done by the finite-volume method as described elsewhere [22]. A segregated implicit solver available in commercial CFD package FLUENT [27] was employed to evaluate the resulting linear system of equations. The condition required for grid convergent results was based on a 1% relative error criterion and the simulations accuracy has been assessed by direct comparison with experimental data. The computational mesh representing the solid cylindrical catalyst of the trickle-bed reactor was created using the integrated solid modelling and meshing program GAMBIT [28] being the representative geometry illustrated in Fig. 1a. All the calculations were carried out on a workstation farm characterized by AMD64 Dual-Core technology.

The CWAO kinetic parameters for the commercial catalyst N-140 were similarly derived to the work developed by Lopes et al. [29]. The right-hand side term of Eq. (9), $S_{i,q}$, includes the reaction rates in terms of the total organic carbon concentration of the lumped species A, B and C as represented by Eq. (13):

$$-r_{TOC_A} = -\frac{dC_{TOC_A}}{dt} = (k_1' + k_2')C_{TOC_A}$$
$$-r_{TOC_B} = -\frac{dC_{TOC_B}}{dt} = k_3' C_{TOC_B} - k_2' C_{TOC_A} \quad (13)$$

where first order reactions were assumed for each mechanism step of the Generalized Kinetic Model. After integrating these equations a mathematical expression for TOC evolution is obtained in Eq. (14).

$$\frac{C_{TOC}}{C_{TOC_0}} = \frac{k_2'}{k_1' + k_2' - k_3'} e^{-k_3' t} + \frac{k_1' - k_3'}{k_1' + k_2' - k_3'} e^{-(k_1' + k_2')t} \quad (14)$$

The activation energies and the pre-exponential factors were calculated by using the Arrhenius plot for the N-140 kinetic studies. These values were used in the corresponding expressions of

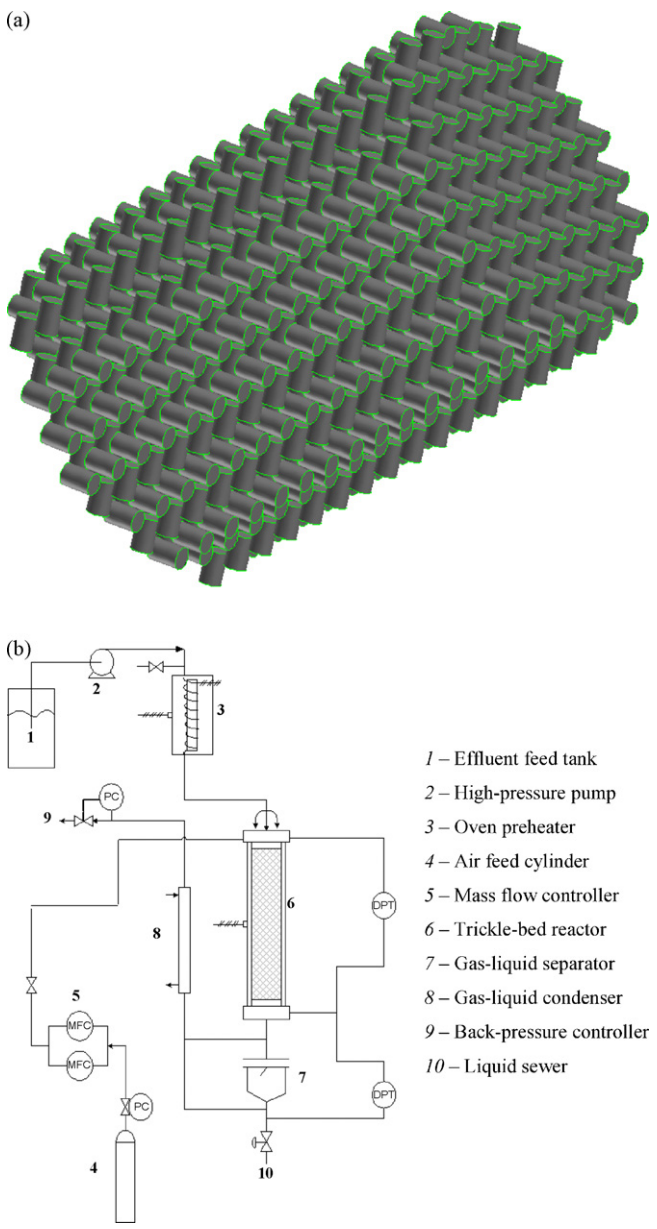

Fig. 1. Schematic diagram of trickle-bed reactor geometry (a) and experimental set-up (b).

the reaction rate constants k'_1, k'_2, k'_3 as functions of temperature, according to Arrhenius law as described in Eq. (15):

$$k'_1 = 452 \exp\left(-\frac{3.121 \times 10^3}{T}\right) \text{ min}^{-1};$$
$$k'_2 = 28.1 \exp\left(-\frac{3.612 \times 10^3}{T}\right) \text{ min}^{-1}; \quad (15)$$
$$k'_3 = 4.32 \times 10^6 \exp\left(-\frac{9.814 \times 10^3}{T}\right) \text{ min}^{-1}$$

Our case study is based on the kinetic studies performed with commercial and laboratory-made catalysts which have been carried out in batch mode operation. Several authors including the recent work developed by Manole et al. [30] indicated that data derived from continuous operation of downflow or upflow flooded-bed reactors exhibited a similar oxidation behaviour to that observed in batch mode, despite very different liquid–solid ratios for the catalytic wet air oxidation of 4-hydroxybenzoic acid.

Table 1
Initial and boundary conditions for the gas and liquid phases.

	$t=0$	$z=0$
α_G	0.625	0.625
α_L	0.375	0.375
G (kg/m^2 s)	0.1–0.7	0.1–0.7
L (kg/m^2 s)	1–15	1–15
P (bar)	30	30
k (m^2/s^2)	Eqs. (16)–(18)	
ε (m^2/s^3)		

The inlet turbulence quantities such as turbulent kinetic energy and turbulent dissipation rate were specified based on FLUENT documentation [27]. The turbulent kinetic energy (k) was estimated from turbulence intensity as expressed in Eq. (16):

$$k = \frac{3}{2}(uI)^2 \quad (16)$$

where I is the turbulence intensity being given by Eq. (17):

$$I = 0.16(Re_{d_H})^{-1/8} \quad (17)$$

The turbulent dissipation rate (ε) was estimated from the turbulent viscosity ratio as expressed by Eq. (18):

$$\varepsilon = \rho C_\mu \frac{k^2}{\mu}\left(\frac{\mu_t}{\mu}\right)^{-1} \quad (18)$$

where C_μ is an empirical constant specified in the turbulence model (0.09). At 30 bar and 200 °C, the inlet turbulent kinetic energies for the liquid (u_L = 0.0055 m/s) and gas phase (u_G = 0.020 m/s) were 0.518 and 8.117 mm^2/s^2, respectively, whereas the turbulent dissipation rates were 0.0654 and 2.934 mm^2/s^3.

Initial and boundary conditions for the gas and liquid phases are systematized in Table 1, whereas the relevant gas and liquid thermophysical properties at P = 30 bar used in the VOF simulations are summarized in Table 2. In Eq. (8), S_h includes sources of enthalpy due to chemical reaction of phenolic compounds: −3000 kJ/mol [31]. Water properties, dissolved oxygen, phenolic compound diffusion coefficients, water and gas heat capacities, water heat of evaporation, heats of reaction, water vapour pressure and water density have been obtained from data or methods included in Reid et al. [31]. Henry constants for oxygen solubility in water were taken from Himmelblau [32]. Phenolic compound and oxygen molecular diffusion coefficients have been also estimated by the methods of Wilke and Chang [33] and Siddiqi–Lucas [34]. Effective diffusion coefficient of pollutant in water and gaseous oxygen–solid mass transfer coefficient has been estimated from Piché et al. [35]. Phenolic compound liquid–solid mass transfer coefficient has been calculated from Goto and Smith [15] and gaseous oxygen–liquid volumetric mass transfer coefficient has been derived from Iliuta et al. [36].

Computations are time dependent and were carried out until steady-state conditions were reached. Standard wall functions were employed for turbulent flow conditions. Although FLUENT

Table 2
Relevant thermophysical properties of gas and liquid phases at P = 30 bar.

Properties	Value (P = 30 bar)		Units
	T = 25 °C	T = 200 °C	
Liquid phase			
Viscosity	8.925×10^{-4}	1.340×10^{-4}	Pa s
Density	998.4	866.9	kg/m^3
Surface tension	7.284×10^{-2}	3.770×10^{-2}	N m
Gas phase			
Viscosity	1.845×10^{-5}	2.584×10^{-5}	Pa s
Density	35.67	21.97	kg/m^3

documentation [27] recommends a range of 30–50 for the cell thickness (y^+), in packed-bed flow it is almost impossible to meet the y^+ criterion everywhere on the sphere surface so that this value computed by the CFD solver was always below 200. Until liquid reaches the outlet, the time step is very low, 10^{-7} s. The time-stepping strategy depends on the number of iterations by time step needed to ensure very low residuals values all less than 10^{-5}.

3. Experimental

3.1. Materials

Low- to moderate-molecular weight phenolic compounds are known to be the major contributors to the toxicity and the antibacterial activity of olive oil wastewaters. Hence, six phenolic-like compounds were obtained for Sigma–Aldrich to mimic the bactericide behaviour of olive oil processing wastewaters, namely: syringic, vanillic, 3,4,5-trimethoxybenzoic, veratric, protocatechuic and *trans*-cinnamic acid. The simulated effluent was prepared through an aqueous solution with 200 ppm for each phenolic acid. Following the screening studies performed in batch mode, a commercial catalyst CuO–MnO_x (N-140: CuO-22%; MnO_x-50%) available from the Süd-Chemie Group, Munich was employed throughout the trickle-bed reactor studies. N-140 catalyst was provided as cylindrical pellets with regular dimensions and bulk density 0.9 kg/L.

3.2. Equipment

The trickle-bed reactor studies have been carried out in our pilot plant as illustrated in Fig. 1b comprising a cylindrical reactor in stainless steel (SS-316) with 50 mm of internal diameter and 1.0 m length. A gas–liquid distributor is attached at the top of the vertical column to promote a better multiphase flow distribution at the reactor inlet. In order to maintain the flux of both phases approximately uniform over the cross-sectional area, the liquid distributor was designed with 60 capillary tubes (0.12 and 0.3 mm internal and outlet diameter, respectively). The capillaries are held between two plates 1 cm apart. The bottom plate has circular holes around the capillaries: the holes are slightly larger in diameter than the outer diameter of the capillary tubes. The gas phase was introduced into the chamber formed between the plates, and exited the distributor through these holes. The top of the packing was 0.5 cm below the distributor, while the packing itself was kept in place by a stainless steel mesh placed at the bottom of the column. A gas–liquid separator is connected to the bottom of the trickle-bed reactor.

An upstream electronic mass flow controller and a downstream electronic backpressure controller (*Brooks* 5866 series with maximum pressure operation of 100 bar) were used to obtain and maintain the desired flow of gas and operating pressure. The pressure drop across the packed bed was measured with a high-pressure differential transducer, which was connected to the top and the bottom of the reactor bed. The liquid phase was delivered to the reactor by a high-pressure *Dosapro Milton Roy* (model XB140K5A100 – SS 316) and can work up to 100 bar and 114 L/h, while the gas phase was delivered to the reactor from high-pressure gas cylinders. The liquid feed was preheated by an external oven from *Carbolite Peak Series* PN120 1500 W equipped with a PID controller for temperature stability ±0.5 K and seven electrical heating jackets (800 W) were attached to the trickle-bed reactor wall.

Total organic carbon was measured with a *Shimadzu 5000 TOC Analyser*, which operates based on the combustion/nondispersive infrared gas analysis method. The parameter uncertainty in TOC measurement, quoted as the deviation of three separate measurements, was never larger than 2% for the range of the TOC concentrations.

3.3. Experimental procedure

The liquid feed was preheated at the temperature set-point (160, 200 °C) and pure air (99.999%) was used as the oxygen source and flowed from the rack of gas cylinders through the mass flow controller into the top of the reactor in where it was *mixed* with the phenolic acids solution feed at the gas–liquid distributor before entering the reactor. The trickle-bed reactor configuration was such that the feed passed over a short bed (length: 5 cm) of inert glass beads before entering the catalyst zone. After exiting the reactor the effluent was cooled and depressurized.

The reactor was loaded with 0.9896 kg of N-140 catalyst and ran continuously until the completion of the flow reactor studies. In order to avoid disruptive cooling/heating and reactor shutdown water was run through the reactor during extended periods when no data were collected. Liquid flow rate was maintained constant in the range 1–10 kg/m^2 s and the air inlet flow rate was fixed in the range 0.1–0.7 kg/m^2 s which allows one to operate in the trickling flow conditions. The flow rates were kept constant throughout the trickle-bed studies in order to maintain consistent hydrodynamics (liquid holdup and two-phase pressure drop) in the reactor to eliminate side effects such as natural pulsing flow that would exist at the upper values for the gas and liquid flow rates. Space time was monitored until the steady-state conversion was reached in terms of total organic carbon removal. Pressure was maintained at approximately 30 bar while the temperature range studied was from 160 to 200 °C. The temperature along the different axial points of the reactor was monitored by means of six *Omega* thermocouples (*K*-type) inserted in one single rod with 5 mm diameter in the radial centre of the reactor.

4. Results and discussion

4.1. Eulerian hydrodynamic validation

The Eulerian framework has been proposed to model trickle-bed reactors at elevated pressures on the prediction of the hydrodynamic parameters pressure drop and liquid holdup. At non-reacting flow conditions, the accuracy of three-dimensional simulations was studied following the successive refinement of tetrahedral meshes. Lopes and Quinta-Ferreira [20] ascribed the effect of packing size on the pressure drop and liquid holdup by different specific surface area of the packing material used in the trickle-bed reactor. It was found that the packing characteristics affect the gas and liquid velocity being the influence of gas velocity prominent at higher superficial gas mass velocities. In this ambit, the theoretical calculations pointed out how the interphase phenomena affected the integral hydrodynamic parameters revealing again the major effect of the gas phase in trickling flow conditions.

The application of different turbulence models including standard, realizable and RNG k–ε models as well as RSM for the hydrodynamics simulation of high-pressure trickle-bed reactor was evaluated thoroughly with the Eulerian multiphase model. On the parametric optimization of several numerical solution parameters, the CFD calculations were examined in terms of tetrahedral mesh size, time step, convergence criteria and discretization schemes. Lopes and Quinta-Ferreira [22] found that coupling a *monotonic upwind scheme for conservation laws* (MUSCL) with a standard k–ε dispersed turbulence can reduce the numerical dispersion that arose in the multiphase flow simulations and, concomitantly, giving the better compromise between numerical accuracy and computational expenditure.

Aiming to investigate the multiphase flow distribution phenomena at high-pressure operation, Lopes and Quinta-Ferreira [21] performed several Eulerian computations with different gas–liquid distributors. The interstitial phenomena were investigated through time averaged axial and radial profiles of liquid holdup and two-phase pressure drop and it was found that liquid flow rate had more prominent effect on radial pressure drop at higher values. Additionally, the gas flow rate had a pronounced influence at lower interaction regimes and the increase of operating pressure on multiphase flow distribution was found to smooth the radial profiles for both hydrodynamic parameters. After performing the Eulerian hydrodynamic validation at non-reacting flow conditions, those optimum numerical solution parameters were integrated into the multiphase flow model aiming to evaluate the axial and radial mapping of reaction parameters (temperature and total organic carbon concentration) in the catalytic wet air oxidation of phenolic wastewaters.

4.2. Reaction studies

Gas–liquid flow inside the TBR was simulated using the Eulerian CFD model and the predicted flow field (velocities and volume fractions of different phases) was further used to solve species transport equations on the simulation of the pollution abatement in the trickle-bed reactor. Aiming to evaluate the dynamic behaviour of the trickle-bed reactor under reacting flow conditions, several Eulerian CFD computations were performed on the catalytic wet air oxidation of phenolic wastewaters. Each simulation is characterized by the axial and radial total organic carbon concentration and temperature profiles obtained for the trickle-bed reactor startup until the steady-state was reached. In this ambit, an initial perturbation on the inlet total organic carbon concentration and/or temperature was accomplished and the dynamic response of the trickle-bed reactor predicted by the CFD model is compared against the experimental data on bulk temperature and TOC conversions.

In order to replicate computationally the TBR oxidation startup, the reactor was firstly heated at the wall temperature (T_w = 160 and 200 °C) and at the time t^* = 0, the feed stream entered the reactor representing a step change in the inlet total organic carbon concentration. High-order discretization scheme (MUSCL) has been employed both for the Eulerian momentum balance equation and the continuity species conservation equation so as to avoid the "numerical diffusion" that arose during the CFD simulations.

4.2.1. Axial total organic carbon profiles

Figs. 2 and 3 show the transient axial profiles predicted by Eulerian CFD model of the mean radial values of the bulk-phase total organic carbon concentration for $T_0 = T_w$ = 160 and 200 °C, respectively. As expected, the increase of temperature led to higher TOC decontamination rates since the catalytic wet air oxidation follows the Arrhenius law. At $T_0 = T_w$ = 160 °C, the TOC conversions were 75.5, 76.8, 77.8, 78.7, 79.3 and 82.0% for t^* = 1, 2, 4, 6, 8, 10 as shown in Fig. 2. If one increases the wall/inlet temperature up to $T_0 = T_w$ = 200 °C, the TOC conversions are increased to 82.3, 82.8, 83.2, 83.6, 83.8 and 84.8% at t^* = 1, 2, 4, 6, 8, 10, respectively. Therefore, the steady-state was reached at t^* = 10 for both operating temperatures, specifically 82.0 and 84.8% for $T_0 = T_w$ = 160 and 200 °C, respectively. According to these axial concentration profiles, the Eulerian model overpredicted slightly the experimental data on TOC removal for both simulated wall/inlet temperatures at steady-state.

Additionally, the Eulerian computations carried out so far [21] have determined a two-phase frictional pressure drop equal to 13 kPa/m, hence the CFD simulations can be roughly considered as isobaric and this fact affected both simulated temperatures.

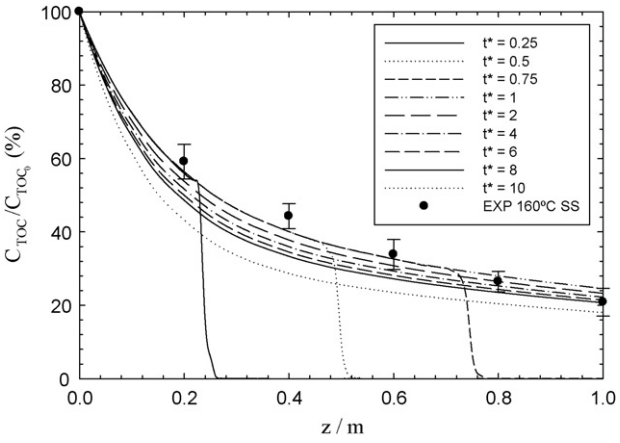

Fig. 2. Mean radial bulk total organic carbon profiles for axial coordinate at transient conditions for different operating dimensionless times, t^* (τ = 195 s, $T_0 = T_w$ = 160 °C, L = 5 kg/m^2 s, G = 0.5 kg/m^2 s, P = 30 bar).

Notwithstanding, the Eulerian model agreed better with experimental data at higher temperatures meaning that another hydrodynamic parameters are impelling the reaction behaviour. This fact can be explained through the homogeneous spatial distribution of liquid fraction achieved at T = 200 °C [22] that in turn yielded a superior mineralization degree in comparison to the lowest temperature. In fact, the higher the temperature, the better the catalyst wetting efficiency is according to the literature. Since the liquid distribution affects mainly the wetting efficiency, then the Eulerian model predicted the experimental data on TOC reduction with a better confidence level. The catalyst wetting efficiency was computed on-time through pre- and post-processing examination activities at several flow times. As the packed-bed flow was simulated under unsteady-state, the calculation procedure was based on auxiliary report function through the computation of the surface integral of catalyst particles that were in contact with liquid phase. This operation was performed periodically and the mean value for the catalyst wetting efficiency was around 82% at L = 5 kg/m^2 s, G = 0.5 kg/m^2 s, P = 30 bar.

As it can be seen through the comparison of the axial total organic carbon concentration profiles shown in Figs. 2 and 3, there is no reasonable difference between the axial TOC profiles obtained at t^* = 1 and t^* = 10 (steady-state) for the highest simulated temperature ($T_0 = T_w$ = 200 °C). In fact, the experimental data lie over the CFD profiles when the wall/inlet temperature was 200 °C;

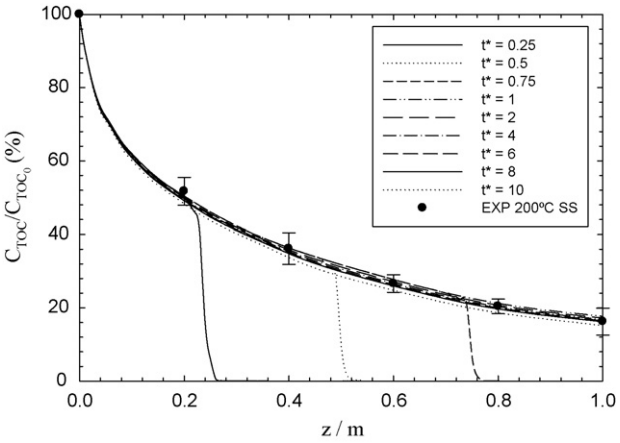

Fig. 3. Mean radial bulk total organic carbon profiles for axial coordinate at transient conditions for different operating dimensionless times, t^* (τ = 195 s, $T_0 = T_w$ = 200 °C, L = 5 kg/m^2 s, G = 0.5 kg/m^2 s, P = 30 bar).

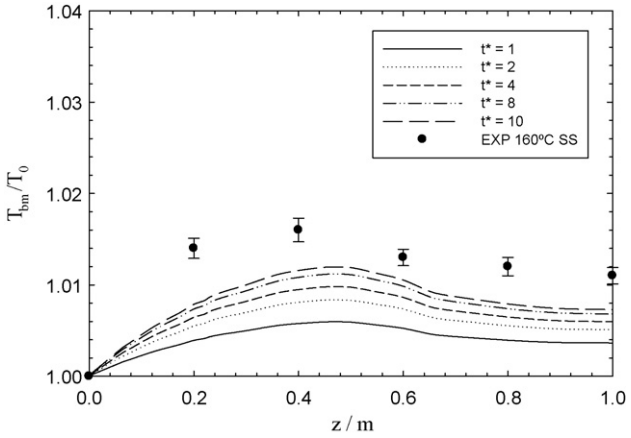

Fig. 4. Mean radial bulk temperature profiles for axial coordinate at transient conditions for different operating dimensionless times, t^* (τ = 195 s, $T_0 = T_w$ = 160 °C, L = 5 kg/m^2 s, G = 0.5 kg/m^2 s, P = 30 bar).

notwithstanding a remarkable difference was detected when the catalytic wet air oxidation was simulated with a wall/inlet temperature 160 °C. Although the qualitative behaviour of TBR was almost the same with both simulated temperatures, it should be pointed that the backmixing degree was higher at $T_0 = T_w$ = 200 °C and the relative errors between computed TOC conversions and experimental data were higher for the lowest simulated temperature ($T_0 = T_w$ = 160 °C).

4.2.2. Axial temperature profiles

Figs. 4 and 5 show the influence of the operating temperature on the computed thermal profiles and experimental data attained for the catalytic wet air oxidation of phenolic wastewater. If one compares the axial temperature and total organic carbon concentration profiles previously shown in Figs. 2 and 3, it can be concluded that the operation time required for the thermal wave and for the TOC wave to achieve the steady-state is roughly the same, t^* = 10. Conversely, the Eulerian CFD model underpredicted the temperature elevation in comparison with the experimental data obtained for both operating temperatures. At the lowest temperature ($T_0 = T_w$ = 160 °C), the axial temperature profiles computed by the Eulerian CFD model indicated that the hotspot is located nearly the axial centre of the trickle-bed reactor (z = 0.45 m) whereas the CFD simulation performed at the highest temperature revealed that the hotspot was achieved earlier (z = 0.36 m). None of the simulated operating temperatures in the catalytic wet air oxidation have shown a superior quantitative prediction on the TBR axial temperature being achieved almost the same the relative errors between the computed results and the experimental data. The maximum differences between computed results and experimental data represented by the error bars in Figs. 2–5 were 8.4 and 3.8%, respectively. Additionally, the major difference between the Eulerian axial temperature profiles shown in Figs. 4 and 5 can be depicted from the intensity of the maximum mean radial bulk temperature. When the CFD simulation was carried out at $T_0 = T_w$ = 160 °C the maximum temperature was 161.9 °C and increased up to 203.2 °C at $T_0 = T_w$ = 200 °C. This fact is directly related with the positive effect of wall/inlet temperature on the catalytic wet air oxidation so that the TOC oxidation rate was promoted by the temperature increase from 160 to 200 °C. One should also bear in mind that the saturated oxygen concentration raises significantly with both increased temperature and oxygen partial pressure in the operating range typical for wet air oxidation. Taking into account that the present CFD simulations were performed at isobaric conditions, a temperature increase from 160 to 200 °C increased oxygen solubility in water at these conditions providing a strong driving force for mass transfer and caused a sharper elevation for the bulk temperature also supported by the experimental data in Fig. 5.

4.2.3. Radial total organic carbon profiles

Fig. 6 shows the transient radial profiles of total organic carbon concentration predicted by the Eulerian CFD model at $T_0 = T_w$ = 160 °C and z = 0.45 m, while Fig. 7 shows the radial total organic carbon concentration profiles obtained at $T_0 = T_w$ = 200 °C and z = 0.36 m. According to Fig. 6, the radial concentration profiles exhibited 5.0% of difference between the TBR centre and the wall at the steady-state and $T_0 = T_w$ = 160 °C. In fact, if one increases the wall/inlet temperature up to 200 °C the difference of total organic carbon conversions between these radial coordinates became 7.6% which reinforces the poor radial mixing effects attained at the hotspot zone. The qualitative behaviour shown by the radial TOC profiles obtained by the CFD model at different temperatures was roughly analogous to the parabolic velocity distribution that characterizes pipe flow. In fact, the higher TOC conversions achieved at the trickle-bed reactor centre can be further sustained by the gas–liquid interaction forces that enable and improve a better multiphase flow distribution and by the higher temperature that endorses higher TOC removal efficiencies.

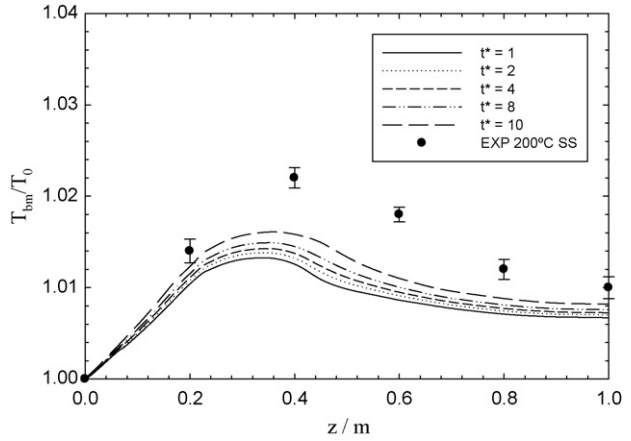

Fig. 5. Mean radial bulk temperature profiles for axial coordinate at transient conditions for different operating dimensionless times, t^* (τ = 195 s, $T_0 = T_w$ = 200 °C, L = 5 kg/m^2 s, G = 0.5 kg/m^2 s, P = 30 bar).

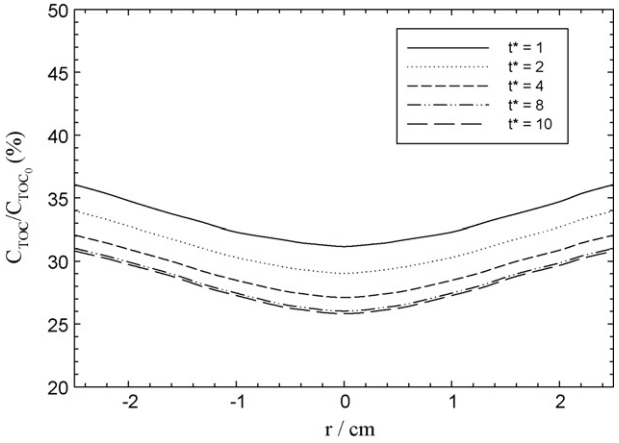

Fig. 6. Radial total organic carbon profiles at the hot spot for different operating dimensionless times, t^* (τ = 195 s, $T_0 = T_w$ = 160 °C, L = 5 kg/m^2 s, G = 0.5 kg/m^2 s, P = 30 bar).

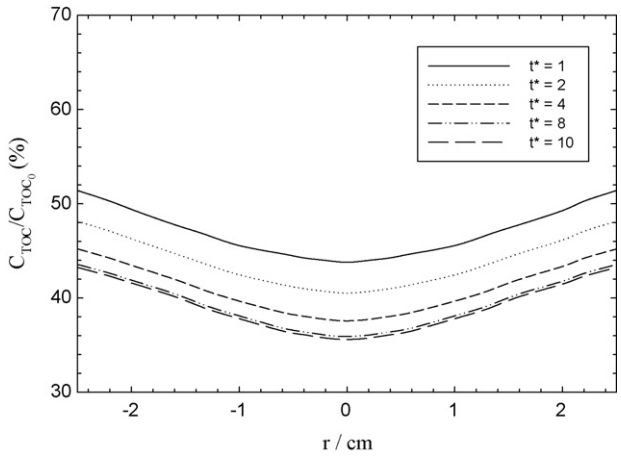

Fig. 7. Radial total organic carbon profiles at the hot spot for different operating dimensionless times, t^* (τ = 195 s, $T_0 = T_w$ = 200 °C, L = 5 kg/m^2 s, G = 0.5 kg/m^2 s, P = 30 bar).

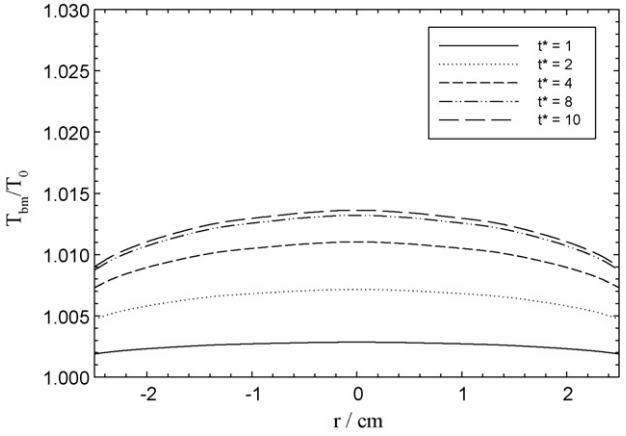

Fig. 8. Radial temperature profiles at the hot spot for different operating dimensionless times, t^* (τ = 195 s, $T_0 = T_w$ = 160 °C, L = 5 kg/m^2 s, G = 0.5 kg/m^2 s, P = 30 bar).

4.2.4. Radial temperature profiles

Figs. 8 and 9 represent the transient radial temperature profiles computed at the hot spot zone, z = 0.45 and 0.36 m, at $T_0 = T_w$ = 160 and 200 °C, respectively. As already advanced in the discussion of radial TOC profiles, the radial temperature distribution was identical for both simulated wall/inlet temperatures. According to Fig. 8, the maximum temperature obtained at $T_0 = T_w$ = 160 °C was 162.2 °C which is comparable to the value already obtained for the axial temperature profile at the same operating temperature. It should be stressed out that although the literature-recommended ratio between the trickle-bed reactor length and diameter obeys to the relation (reactor length/reactor diameter) ≤20, an equivalent temperature elevation was computed by the Eulerian CFD model for the axial and radial temperature profiles. The increase of wall/inlet temperature up to 200 °C generated a maximum temperature difference of 3.7 °C between the TBR centre and wall at the hotspot which was also similar to the difference attained along the axial coordinate.

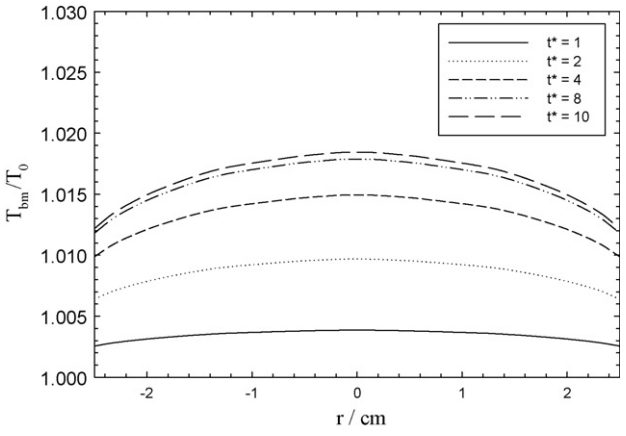

Fig. 9. Radial temperature profiles at the hot spot for different operating dimensionless times, t^* (τ = 195 s, $T_0 = T_w$ = 200 °C, L = 5 kg/m^2 s, G = 0.5 kg/m^2 s, P = 30 bar).

After the comparison between the radial total organic carbon concentration and temperature profiles plotted in Figs. 6–9, it can be observed that TOC concentration is decreasing from the wall to the centre whereas the bulk temperature is increasing from the reactor wall to the centre. This fact can be explained by the chemical reaction thermodynamics which promotes higher TOC decontamination rates at elevated temperatures. Notwithstanding, the Eulerian CFD simulations performed at $T_0 = T_w$ = 160 and 200 °C indicated that steady-state was reached roughly at t^* = 10.

5. Conclusions

Aiming to investigate the dynamic behaviour of a pilot trickle-bed reactor, an Eulerian CFD model was developed to simulate the gas–liquid flow through a catalytic bed of cylindrical particles. Following the hydrodynamic corroboration, the Eulerian CFD model was validated with experimental data taken from a trickle-bed reactor pilot plant specifically designed for the catalytic wet oxidation of low- to moderate strength wastewaters.

Several computational runs were carried out at unsteady-state operation in order to evaluate the dynamic performance addressing the total organic carbon concentration and temperature profiles. Backmixing phenomena were detected for both simulated operating temperatures. The effect of operating temperature was examined in terms of axial/radial TOC and temperature profiles. During the CFD model validation at the higher operating temperature, the Eulerian model was found to predict better the TOC removal efficiency than for the lower operating temperature. However, the axial bulk temperature profiles have not shown the same confidence level of temperature prediction as demonstrated in the axial TOC conversion profiles. Nevertheless, the Eulerian CFD framework is envisaged as a valuable tool to accelerate the industrial implementation of trickle-bed reactors in advanced wastewater treatment plants.

Acknowledgments

The authors gratefully acknowledged the financial support of REMOVALS – 6th Framework Program for Research and Technological Development – FP06 Project no. 018525 and *Fundação para a Ciência e Tecnologia*, Portugal.

References

[1] J.G. Collin, G.L. Puma, A. Bono, D. Krishnaiah, Sonophotocatalysis in advanced oxidation process: a short review, Ultrasonics Sonochemistry 16 (2009) 583–589.
[2] F.J. Rivas, M. Carbajo, F. Beltrán, O. Gimeno, J. Frades, Comparison of different advanced oxidation processes (AOPs) in the presence of perovskites, Journal of Hazardous Materials 155 (2008) 407–414.
[3] M. Zhou, J. He, Degradation of azo dye by three clean advanced oxidation processes: wet oxidation, electrochemical oxidation and wet electrochemical oxidation—a comparative study, Electrochimica Acta 53 (2007) 1902–1910.
[4] P. Cañizares, J. Lobato, R. Paz, M.A. Rodrigo, C. Sáez, Advanced oxidation processes for the treatment of olive-oil mills wastewater, Chemosphere 67 (2007) 832–838.

[5] A. Mandal, A.K. De, S. Bhattacharjee, Removal of catechol from aqueous solution by advanced photo-oxidation process, Chemical Engineering Journal 102 (2004) 203–208.
[6] M. Pera-Titus, V. García-Molina, M.A. Baños, J. Giménez, S. Esplugas, Degradation of chlorophenols by means of advanced oxidation processes: a general review, Applied Catalysis B: Environmental 47 (20) (2004) 219–256.
[7] S. Esplugas, J. Giménez, S. Contreras, E. Pascual, M. Rodríguez, Comparison of different advanced oxidation processes for phenol degradation, Water Research 36 (2002) 1034–1042.
[8] S.K. Bhargava, J. Tardio, J. Prasad, K. Foger, D.B. Akolekar, S.C. Grocott, Wet oxidation and catalytic wet oxidation, Industrial and Engineering Chemistry Research 45 (2006) 1221–1258.
[9] A. Pintar, J. Levec, Catalytic liquid-phase oxidation of phenol aqueous solutions. A kinetic investigation, Industrial and Engineering Chemistry Research 33 (1994) 3070–3077.
[10] F. Stüber, I. Polaert, H. Delmas, J. Font, A. Fortuny, A. Fabregat, Catalytic wet air oxidation of phenol using active carbon: performance of discontinuous and continuous reactors, Journal of Chemical Technology Biotechnology 76 (2001) 743–751.
[11] C.B. Maugans, A. Akgerman, Catalytic wet oxidation of phenol in a trickle bed reactor over a Pt/TiO_2 catalyst, Water Research 37 (2003) 319–328.
[12] A. Pintar, M. Besson, P. Gallezot, Catalytic wet air oxidation of kraft bleach plant effluents in a trickle bed reactor over a Ru/TiO_2 catalyst, Applied Catalysis B: Environmental 31 (2001) 275–290.
[13] V. Tukac, J. Vokál, J. Hanika, Mass transfer limited wet oxidation of phenol, Journal of Chemical Technology Biotechnology 76 (2001) 506–510.
[14] A. Fortuny, C. Bengoa, J. Font, F. Castells, A. Fabregat, Water pollution abatement by catalytic wet air oxidation in a trickle bed reactor, Catalysis Today 53 (1999) 107–114.
[15] S. Goto, J.M. Smith, Trickle-bed reactor performance part II. Reaction studies, AIChE Journal 21 (1975) 714–720.
[16] A. Chander, A. Kundu, S.K. Bej, A.K. Dalai, D.K. Vohra, Hydrodynamic characteristics of cocurrent upflow and downflow of gas and liquid in a fixed bed reactor, Fuel 80 (2001) 1043–1053.
[17] A.K. Saroha, R. Khera, Hydrodynamic study of fixed beds with cocurrent upflow and downflow, Chemical Engineering and Processing 45 (2006) 455–460.
[18] M.P. Dudukovic, F. Larachi, P.L. Mills, Multiphase catalytic reactors: a perspective on current knowledge and future trends, Catalysis Reviews: Science and Engineering 44 (2002) 123–246.
[19] P.R. Gunjal, V.V. Ranade, Modeling of laboratory and commercial scale hydroprocessing reactors using CFD, Chemical Engineering Science 62 (2007) 5512–5526.
[20] R.J.G. Lopes, R.M. Quinta-Ferreira, Three-dimensional numerical simulation of pressure drop and liquid holdup for high-pressure trickle-bed reactor, Chemical Engineering Journal 145 (2008) 112–120.
[21] R.J.G. Lopes, R.M. Quinta-Ferreira, CFD modelling of multiphase flow distribution in trickle beds, Chemical Engineering Journal 147 (2009) 342–355.
[22] R.J.G. Lopes, R.M. Quinta-Ferreira, Turbulence modelling of high-pressure trickle-bed reactor, Chemical Engineering Science 64 (2009) 1806–1819.
[23] M.H. Al-Dahhan, F. Larachi, M.P. Dudukovic, A. Laurent, High pressure trickle-bed reactors: a review, Industrial and Engineering Chemistry Research 36 (1997) 3292–3314.
[24] A. Attou, G.A. Ferschneider, Two-fluid model for flow regime transition in gas–liquid trickle-bed reactors, Chemical Engineering Science 54 (1999) 5031–5037.
[25] F. Larachi, M. Cassanello, A. Laurent, Gas–liquid interfacial mass transfer in trickle-bed reactors at elevated pressures, Industrial and Engineering Chemistry Research 37 (1998) 718–733.
[26] S. Elghobashi, T. Abou-Arab, M. Rizk, A. Mostafa, Prediction of the particle-laden jet with a two-equation turbulence model, International Journal of Multiphase Flow 10 (1984) 697–710.
[27] FLUENT 6.1., User's Manual to FLUENT 6.1, Fluent Inc., Centrera Resource Park, 10 Cavendish Court, Lebanon, USA, 2005.
[28] GAMBIT 2, User's Manual to GAMBIT 2, Fluent Inc., Centrera Resource Park, 10 Cavendish Court, Lebanon, USA, 2005.
[29] R.J.G. Lopes, A.M.T. Silva, R.M. Quinta-Ferreira, Screening of catalysts and effect of temperature for kinetic degradation studies of aromatic compounds during wet oxidation, Applied Catalysis B: Environmental 73 (2007) 193–202.
[30] C.C. Manole, C. Julcour-Lebigue, A.M. Wilhelm, H. Delmas, Catalytic oxidation of 4-hydroxybenzoic acid on activated carbon in batch autoclave and fixed-bed reactors, Industrial and Engineering Chemistry Research 46 (2007) 8388–8396.
[31] R.C. Reid, J.M. Prausnitz, B.E. Poling, The Properties of Gases and Liquids, McGraw-Hill, New York, 1987.
[32] D.M. Himmelblau, Solubilities of inert gases in water. 0 °C to near the critical point of water, Journal of Chemical Engineering Data 5 (1960) 10.
[33] C.R. Wilke, P. Chang, Correlation of diffusion coefficients in dilute solutions, AIChE Journal 1 (1955) 264.
[34] M.A. Siddiqi, K. Lucas, Correlations for prediction of diffusion in liquid, Canadian Journal of Chemical Engineering 64 (1986) 839.
[35] S. Piché, F. Larachi, I. Iliuta, B.P.A. Grandjean, Improving the prediction of liquid back-mixing in trickle-bed reactors using a neural network approach, Journal of Chemical Technology Biotechnology 77 (2002) 989.
[36] I. Iliuta, F. Larachi, B.P.A. Grandjean, G. Wild, Gas–liquid interfacial mass transfer in trickle-bed reactors: state-of-the-art correlations, Chemical Engineering Science 54 (1999) 5633.